

Semesterarbeit

Tomography on Superconducting Qubit States

Peter Maurer

maurerpe@student.ethz.ch

Supervisors:

Romeo Bianchetti, Johannes Fink, Peter Leek

Professor:

Andreas Wallraff

Semester work

at the Quantum Device Lab

Laboratory for Solid State Physics, ETH Zürich

February 2007

Abstract:

Quantum State Tomography (QST) has been performed on a superconducting Qubit. The Qubit consists of a Cooper pair box (CPB) coupled to a microwave resonator. Operations on the Qubit's ground state, excited state and two superposition states can be performed by applying microwave pulses. The effects of pulses have been analyzed by mapping the Qubit's projection on the excited state as a function of pulse length and pulse amplitude. This enables us to do QST using only three pulses, the minimal amount in number. In the analysis a calibration procedure takes into account that the pulses are not known perfectly and corrects that for the further analysis. This QST process has been used to trace the Bloch vector in a Ramsey experiment.

Picture credits

Fig. 1.1, 1.2 a), 1.4, 3.1 extracted from Schuster; PhD thesis

Fig. 1.3 extracted from California Institute of Technology [1]

Acknowledgement

My thanks go to Prof. Dr. Andreas Wallraff, Dr. Peter Leek, Romeo Bianchetti and Johannes Fink, for their help and assistance in my Semester Work.

Without their support this work would not have achieved what it has managed to achieve.

I thank Andreas for guiding me into the subject of quantum computing an area of particular interest to me. Peter for helping with recording the data. Indeed the Ramsey measurements would not have been recorded if he had not stayed longer and retried the experiment. Romeo for assisting me, especially in the first week, helping me with the measurement setup and giving me a program to simulate the cavity's response. Johannes for supporting me with the measuring program and recording together with me the calibrations curve for the microwave mixer.

I was fascinated by the subject of quantum computing and the way we are able to play with quantum mechanics on a macroscopic level.

I hope that there will be another occasion for me to join the group again in future.

Picture credits.....	2
Acknowledgement	3
1 Qubit	5
1.1 Cooper pair box.....	7
1.2 Coupling to cavity.....	12
2 Quantum State Tomography.....	19
2.1 Intuitive Approach to Quantum State Tomography.....	20
2.2 Physical Approach to State Tomography	23
3 Experimental setups	28
4 Experiments	31
4.1 Dephasing processes	32
4.2 Serial pulse sequence	34
4.2.1 Simulation.....	34
4.2.2 Results.....	36
4.2.3 Response	38
4.2.4 Pattern files	39
4.3 Parallel pulse sequence	40
4.3.1 Simulation.....	40
4.3.2 Results.....	42
4.3.3 Calibration.....	44
4.3.4 Pattern files	46
4.4 Quantum state tomography using three operations.....	47
4.4.1 Results.....	48
4.4.2 Calibrations.....	52
4.4.2.1 Calibrating the tomography pulses	53
4.4.4 Visibility	56
4.4.5 Pattern files	56
4.5 Ramsey.....	58
4.5.1 Results.....	58
4.5.2 Pattern files	61
References.....	63

1 Qubit

For the first time it is possible to create and manipulate devices which behave totally quantum mechanically. The ability to do so opens a broad avenue of exciting experiments in cavity QED. Superconducting Qubits coupled to a resonator can be addressed by microwave pulses. Over the last years experiments using superconducting Qubits could reproduce results found previously on other systems. It is not unlikely that superconducting Qubits will become one day a system that can be scaled up most easily. However, today superconducting Qubits are still in their initial phase.

In the experiment a superconducting Qubit called cooper pair box (CPB) was used. Cooper pairs are confined to the CPB. The CPB's energy levels are discrete and depend on the number of Cooper pairs on it and the magnetic field. The transition frequencies are in the microwave range. Therefore the CPB is sometime also called an artificial atom. The energy levels are not equidistant, which has the advantage that only one particular transition is addressed directly. Cooper pairs can tunnel from a cooper pair reservoir to the island through Josephson junctions. An energy level's fine tuning can be done by a gate voltage applied to the CPB. As it will be seen the measurements are performed at a particular point.

The CPB is placed in a cavity with a certain resonance frequency which is detuned from the CPB's transition frequency. The electromagnetic field in the cavity induces a dipole

interaction with the CPB ($\sim 10^4$ times larger than the dipole moment of an alkali atom) by moving its Cooper pairs. This couples to the electromagnetic field and induces by absorbing a photon a transitions from the ground state to the excited state and vice versa. The transition rate can be controlled by the detuning.

Since a photon interacts with the CPB, it picks up a phase. This is a good method for readout.

First a brief technical description of the system will be given. The system's Hamiltonian is derived and it is seen that it describes a two level system. The knowledge of the Hamiltonian is important in the discussion on the coupling of the two level system to the cavity.

In a second part the coupling of the CPB to the cavity is discussed. Rabi oscillations are discussed and it is explained how the readout process is realized [6]. The advantage of measuring the phase rather than the amplitude is also discussed.

In these two chapters it is shown that four of the DiVincenzo criteria: unitary operations on the system, preparation of an initial state, readout process and long coherence of the system are fulfilled. Only the scaling up ability will not be mentioned.

1.1 Cooper pair box

The circuit was designed in a way that it consists of a capacitance and a CPB, embedded in a cavity (Fig. 1.1). The cavity is similar to a two dimensional coax cable (see next section). A CPB is placed in the cavity. The CPB is a superconducting island connected to ground by two Josephson junctions.

A Josephson junction is a connection of two superconducting material by an insulator. Cooper pairs can tunnel coherently through the insulator. This restriction on the cooper pairs phase and the fact that the island, the Josephson junctions and the ground form a loop yield to restriction on tunneling current as a function on the external magnetic field (see SQUID [7]).

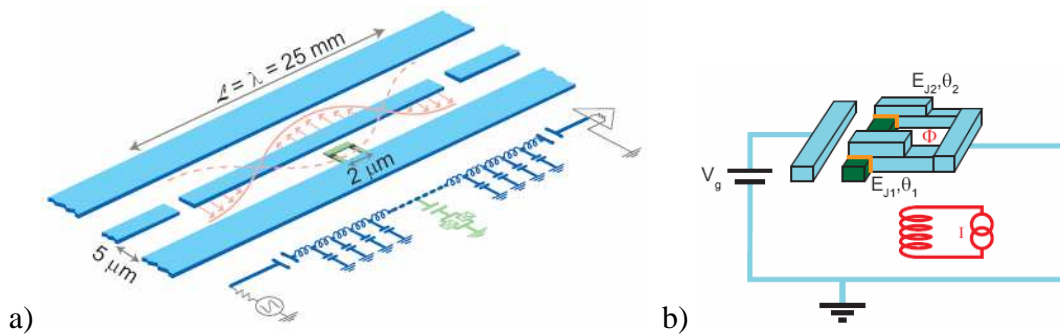


Fig. 1.1 a) Schematic picture of the cavity. The blue areas are conducting. The analogy to a planar coax cable is pictured by the attached circuit diagram. The gap in the middle line is a capacitance which acts as a mirror (analogue to bad connected coax cable).

b) Schematic picture of a Cooper pair Box (CPB) the Josephson junctions are yellow marked. The red coil gives a condition for the phase. A gate V_g give the possibility to control the classical amount of induced charge and change therefore the energy difference between the two levels.

As shown in Fig. 1.1 there is a captive coupling between the CPB and the gate. The induced charge on the CPB can classically be calculated by $n_g = C_g V_g / e$, where V_g is the gate voltage and C_g is the capacity. Further reading can be found in [9].

In quantum mechanics the number of cooper pairs in the CPB is an integer N .

Therefore the Hamiltonian for the electrostatic case can be written as [1]

$$H_{el} = 4E_c (N - n_g)^2$$

where $E_c = e^2 / (2(C_g + C_j))$ is the electrostatic charging energy, with C_j the Josephson capacity.

For this arrangement it can be seen that the energy spectrum consists of non equidistant discrete energy levels, in the basis of cooper pair numbers N . This nonlinearity is crucial for treatment of a two level system.

As a function of the gate voltage the CPB's energy is quadratic and degenerate (at least for the case where the Josephson junction Hamiltonian (see below) is neglected) if n_g is an integer (Fig. 1.2).

For the tunneling process of cooper pairs through the Josephson junction the Hamiltonian

$$H_J = \frac{E_J}{2} \sum_n \cos\left(\frac{\pi\Phi}{\Phi_0}\right) (|n\rangle\langle n+1| + |n+1\rangle\langle n|) - id \sin\left(\frac{\pi\Phi}{\Phi_0}\right) (|n\rangle\langle n+1| - |n+1\rangle\langle n|)$$

can be found [1]. Here E_J is the sum of the Josephson energies, d the fractional difference between the Josephson energies, Φ_0 the flux quantum, Φ the magnetic flux through the loop and $|n\rangle$ the number of cooper pairs in the CPB.

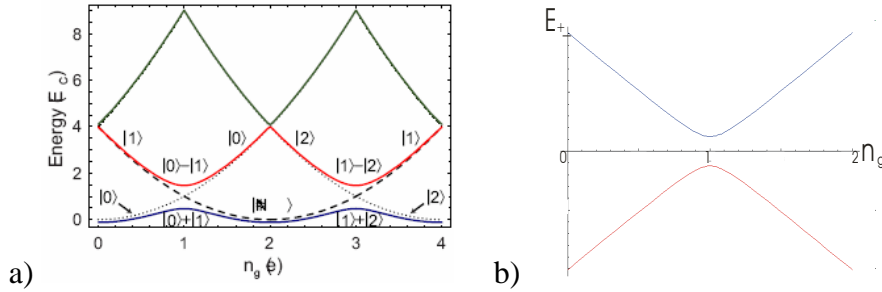


Fig. 1.2 a) Shows calculation for the energy diagram for a CPB in function of the applied gate voltage. A periodicity of even integers of $n_g(e)$ can be seen due to the discrete number of Cooper pairs. A energy level splitting at the degenerated points occurs from a transition between the n and $n+1$ Cooper pairs on the CPB.
b) Shows the plot for the energy levels of a two level system as calculated below.

The Hamiltonian $H = H_{el} + H_J$ in the charge basis can only be solved numerically. Transforming basis $|n\rangle$ to the continuous phase basis $|\theta\rangle$ the eigenvalue problem can be solved analytically [1] (Fig. 1.2 a)).

As it will be seen later on, the Jaynes Cummings Hamiltonian (JCH) describes a two level system in an external electromagnetic field. The JCH is in the charge basis. Therefore the Hamiltonian for the CPB will be solved in the charge basis. For simplification only the first two levels are take in to consideration. This simplification is justified because the experiments are operating at low temperatures ($\approx 20mK$) much lower then the energy level splitting.

If the basis $|0\rangle \cong (0 \ 1)^T$ and $|1\rangle \cong (1 \ 0)^T$ is used, the Hamiltonian can be written as

$$H = -\frac{1}{2} \left(4E_C(1-n_g)\sigma_z + E_J \left(\cos\left(\frac{\pi\Phi}{\Phi_0}\right)\sigma_x + d \sin\left(\frac{\pi\Phi}{\Phi_0}\right)\sigma_y \right) \right)$$

The eigenvalues and eigenfunctions can be calculated analytically

$$E_{\pm} = \pm \frac{1}{2} \sqrt{16E_C^2(1-n_g)^2 + E_J^2 \left(\cos^2\left(\frac{\pi\Phi}{\Phi_0}\right) + d^2 \sin^2\left(\frac{\pi\Phi}{\Phi_0}\right) \right)}$$

and an energy diagram like Fig. 1.2 b) results.

This energy level splitting is similar to the energy level splitting in a quantum mechanical double well potential. In a quantum mechanical double well potential an large energy level splitting occurs if the energy barrier between the two wells is low and vice versa.

In the case of the CPB the energy barrier can easily be adjusted by varying n_g .

Two simple cases can be seen. In the point $n_g=0$ the Eigenfunctions are given by $|0\rangle$ and $|1\rangle$, where the assumption $E_C \gg E_J$ was made. For $n_g=1$ the Eigenfunction are $|0\rangle + e^{i\varphi}|1\rangle$ and $|0\rangle - e^{i\varphi}|1\rangle$. The fix phase $e^{i\varphi}$ is of no interest because we have in the beginning a rotational degree of freedom around the z_axis.

During the experiment one would like to keep the system at a particular detuning frequency. Therefore the energy level difference has to stay constant.

Fluctuations in the gate charge can occur and will change the n_g and the detuning frequency. The lowest sensitivity in a change of n_g is at n_g even integer of e and the noise is therefore in second order of n_g . Therefore the operations point is chosen as n_g odd integer of e .

1.2 Coupling to cavity

As we have seen in the previous section the CPB can be treated as a two level system. Dipole interaction between the CPB's island and the electromagnetic field in the cavity allows interactions at a rate g between the CPB and the cavity.

The CPB in a cavity is a system where a photon can (theoretically) turn into an excited state of the CPB and vice versa. However in this chapter, it will be proved that for our experiment (large detuning) the probability for such a transition will vanish.

Additionally the two level system can decay at a rate γ_{\perp} into a mode not captured by the resonator. The cavity has also a finite lose which allows photons to escape by a rate κ . The γ_{\perp} decay is the reason why the system is dissipative. However the dissipative processes are on a time scale of μs , while the operation will be on timescales of $10 ns$.

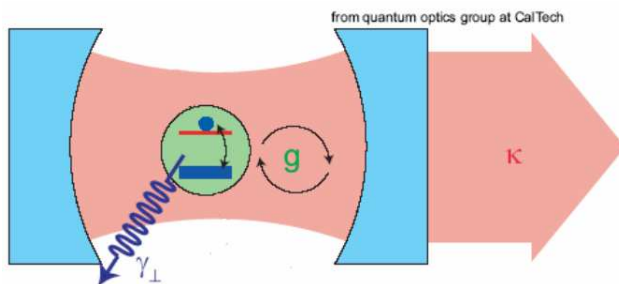


Fig. 1.3 Schematic of a cavity and a two level system. The two level system couples to the cavity's electromagnetic field at the rate g . Decoherence is caused by the decay into modes which are not captured by the cavity or by photons being transmitted through the mirrors.

Neglecting dissipative processes the Hamiltonian for such a process is called Jaynes Cummings Hamiltonian (JCH)

$$H_{JC} = \hbar\omega_r \left(a^\dagger a + \frac{1}{2} \right) + \hbar \frac{\omega_a}{2} \sigma_z + \hbar g (a^\dagger \sigma^- + a \sigma^+).$$

A good derivation can be found in [1] or standard books on quantum mechanic.

The coupling constant is $g = 2 \frac{C_g}{C_g + C_j} \xi \sqrt{\frac{\alpha}{n}} \left(\frac{\mu_r}{\epsilon_r} \right)^{1/4} \omega_r$, with $\xi = 0.4$, n number of nodes. ϵ_r/μ_r are the relative electric/magnetic permeability and α is the fine structure constant. The resonator frequency, transition frequency of the Qubit is ω_r , ω_a respectively.

The first term represents the photon energy stored in the resonator, the second describes the energy of the two level system. The third term consists of a creation of a photon and a transition from the CPB's excited- to its ground state $a^\dagger \sigma^-$, a absorption of a photon and a transition from the CPB's ground - to its excited state $a \sigma^+$ respectively.

First the system's evolution will be discussed.

The evolution of $|\psi\rangle$ is given by of the Schrödinger equation's solution $Exp\left(-\frac{iH_{JC}}{\hbar}t\right)|\psi\rangle$. If the canonic basis $|g,n\rangle \cong e_{2n}$, $|e,n-1\rangle \cong e_{2n+1}$ is used the matrix

representation of H_{JC} can be written in block diagonal form

$$H_{JC} = \hbar \begin{pmatrix} \begin{pmatrix} \omega_r & g \\ g & (\omega_r + \Delta) \end{pmatrix} & & & 0 \\ & \ddots & & \\ & & 0 & \begin{pmatrix} m\omega_r & g\sqrt{m} \\ g\sqrt{m} & (m-1)\omega_r + (\omega_r + \Delta) \end{pmatrix} \end{pmatrix}.$$

(For algebraic reasons it is convenient to use a finite basis. This can also be justified by a finite energy that is available.)

Solving the Schrödinger equation gives

$$\text{Exp}\left(-\frac{iH_{JC}}{\hbar}t\right) = \begin{pmatrix} \text{Exp}-it \begin{pmatrix} \omega_r & g \\ g & (\omega_r + \Delta) \end{pmatrix} & & & 0 \\ & \ddots & & \\ & & 0 & \text{Exp}-it \begin{pmatrix} m\omega_r & g\sqrt{m} \\ g\sqrt{m} & (m\omega_r + \Delta) \end{pmatrix} \end{pmatrix}$$

An analogy between the propagator above and the propagator for neutrinos can be seen (where the propagator in the Basis $e_1 \equiv |n_e\rangle$ and $e_2 \equiv |n_\mu\rangle$ is given as $\begin{pmatrix} \cos^2(\theta) - \text{Exp}[2iEt]\sin^2(\theta) & \cos(\theta)\sin(\theta) + \text{Exp}[2iEt]\cos(\theta)\sin(\theta) \\ -\cos(\theta)\sin(\theta) - \text{Exp}[2iEt]\cos(\theta)\sin(\theta) & \text{Exp}[2iEt]\cos^2(\theta) - \sin^2(\theta) \end{pmatrix}$, where θ is the mixing angle and $E = m_\mu^2 - m_e^2$, with $\hbar=1$ and $c=1$). Therefore oscillations between $|g, n\rangle$ and $|e, n-1\rangle$ are similar like oscillations from one neutrino flavor to another. And the detuning is analogous to the mixing angle.

The probability that a photon induced a transition from the CPB's ground state to its excited state is given by

$$p_{g,e} = \left| \langle e, n-1 | \text{Exp}\left(-\frac{iH_{JC}}{\hbar}t\right) | g, n \rangle \right|^2 = \frac{g^2 n \sin^2\left(t\sqrt{4g^2n + \Delta^2}\right)}{4g^2n + \Delta^2}$$

In Δ this is a modulated Lorentzian function. Indeed the cross section goes to zero with $1/\left(4 + \left(\Delta/(g\sqrt{n})\right)^2\right)$ (with $g \ll \Delta$ and small n).

If a photon interacts with the CPB it will change its phase, even if it does not get absorbed. The propagator's $\text{Exp}\left(-\frac{iH_{JC}}{\hbar}t\right)$ first element describes the process where the

CPB stays in its ground state. This process has a probability given by

$$\begin{aligned} p_{g,g} &= \left| \langle g, n | \text{Exp}\left(-\frac{iH_{JC}}{\hbar}t\right) | g, n \rangle \right|^2 \\ &= \cos^2\left(t\sqrt{g^2n + \Delta^2}\right) + \frac{1}{(2g/\Delta)^2 n + 1} \sin^2\left(t\sqrt{4g^2n + \Delta^2}\right) \end{aligned}$$

For detuning $g \ll \Delta$ this is much larger and goes to one for large detuning.

According to Schuster the Eigenstates for this Hamiltonian can be written as

$$\begin{aligned} |g, n\rangle &= \cos(\theta_n) |g, n\rangle - \sin(\theta_n) |e, n-1\rangle \\ |e, n-1\rangle &= \sin(\theta_n) |g, n\rangle + \cos(\theta_n) |e, n-1\rangle \end{aligned}$$

Where the angle $\theta_n = \frac{1}{2} \arctan\left(\frac{2g\sqrt{n}}{\Delta}\right)$ is a measure for the hybridization.

Now that we showed that how the system behaves, we have to discuss how the measurements can be done.

If the case of strong detuning $g \ll \Delta \hat{=} \omega_r - \omega_a$ (dispersive lines) is assumed the JCH can be approximated by series expansions in $\frac{g}{\Delta}$ [1] by

$$H_{JC} \approx \hbar \left(\omega_r + \frac{g^2}{\Delta} \sigma_z \right) \left(a^\dagger a + \frac{1}{2} \right) + \hbar \frac{\omega_a}{2} \sigma_z.$$

One can see the stark shift $\hbar \frac{g^2}{\Delta} a^\dagger a \sigma_z$ depending on the photon number and the lamb shift $\hbar \frac{g^2}{2\Delta} \sigma_z$ due to interaction with the vacuum field. Extensive discussion on an atom in an electromagnetic field can be found in [2] or [1].

Due to the stark- and lamb shift a frequency different of $2 \frac{g^2}{\Delta} \left(n + \frac{1}{2} \right)$ can be obtained between ground- and excited state.

This is now used to detect if the system is in its ground or excited state.

The electric field's amplitude in the resonator vs. the frequency has a Lorentzian shape with the maximum at different frequencies (stark-/lamb shift) depending on the CPB's state (Fig. 1.4 a)).

Analogue to classical mechanics the phase has than an arctan shape with a similar shift (Fig. 1.4 b)). The derivation can be found in books on quantum electronics.

It can be shown that the resonance width κ and frequency shift for our particular experiment result in a nearly indistinguishable signal for the ground and excited state.

The difference in the phase on the other hand is much larger (Fig. 1.5).

An extended discussion can be found in [8].

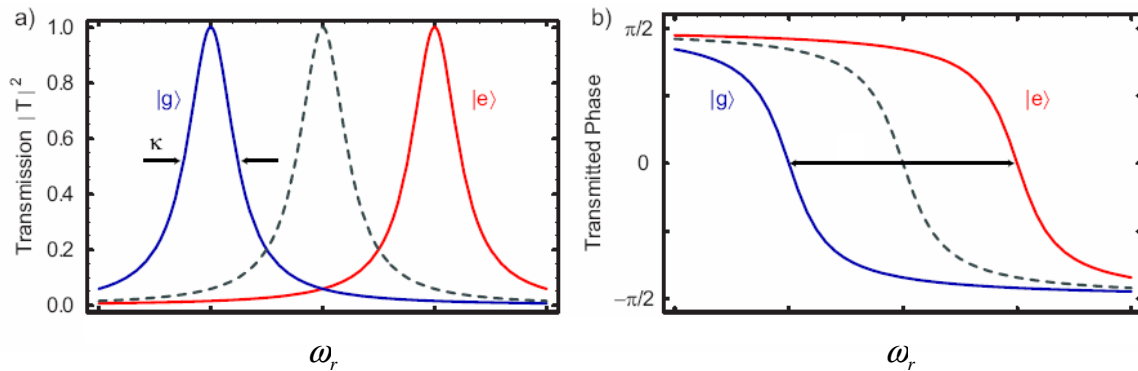


Fig. 1.4 a) Shows the electromagnetic field's amplitude in the resonator. It follows a Lorentzian function. The ground, excited state are indicated by blue, red color respectively.

b) Shows the arctan function for the field's phase.

Two possibilities how the readout process can be realized were discussed and the advantage of phase readout was shown.

Due to relaxation from the excited to the ground state the response follows an exponential.

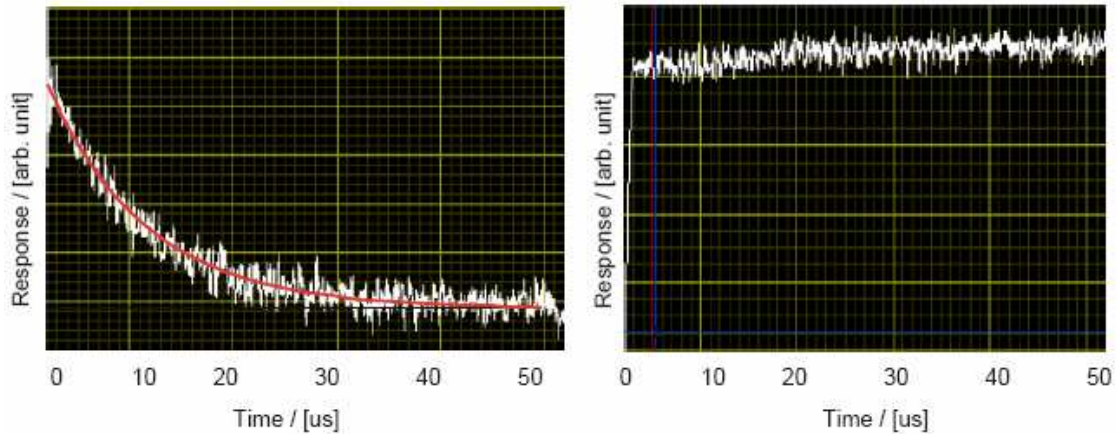


Fig. 1.5 Typical raw data from a measurement. Left shows the response if the phase is measured, right shows the response if the amplitude is measured. It can easily be seen that the response is much larger if the phase is measured.

Indeed one measurement would only gives one of the two Eigenvalues for the response. However an averaging over different measurements yield to the desired expectation value.

Repeating the measurement several times and taking the average gives the expected exponential decay (Fig. 1.5). One can see that the signal noise ratio in the amplitude measurement is very small.

This gives the possibility to determine the projection on the excited state as we will see in Chap. *Experiments*.

2 Quantum State Tomography

In quantum computation it is important to exactly determine an arbitrary state $|\psi\rangle = a|0\rangle + b|1\rangle$.

A measurement projects $|\psi\rangle$ on a particular state given by the experimental setup. The state $|\psi\rangle$ can be prepared several times and therefore the experiment can be repeated many times.

This allows us to determine exactly one component of the Bloch vector but also gives a total uncertainty for the other two components. This is completely analog to spins in quantum mechanics.

However the state $|\psi\rangle$ can theoretically be determined arbitrary exactly by using quantum state tomography (QST). QST determines in three different experiments the projection on three different axis. With this information the state $|\psi\rangle$ can be determined.

Instead of measuring the projection on different axis the Bloch vector can be rotated and than be projected always on the same axis.

In the first section an intuitive geometrical approach to QST will be given. The discussion will be a quite graphical explanation of QST's principles. Therefore this kind of approach will give us some intuitions to see solutions in QST, especially if the rotations axis are perpendicular to each other (i.e. $\text{Tr}(R_i R_j) = 2\delta_{ij}$, with R_i operations on the state). This will be important when the results of the 2D mapping for serial and

parallel pulse sequences will be discussed. A theoretical paper addressing this topic can be found in [5].

On the other hand this treatment is not appropriate to perform calculations. For that reason the problem will be handled mathematically in the second section. This will then be the fundament for the simulations, our measurements, the QST with 3 points and the Ramsey experiment. The advantage of easy mathematical treatment will be paid by losing the graphical argumentation.

2.1 Intuitive Approach to Quantum State Tomography

As showed previous our qubit is realized by a two level system. The qubit's state is then given by $|\psi\rangle = a|0\rangle + b|1\rangle$, where $|0\rangle, |1\rangle$ are orthonormal Eigenstates of the Hamiltonian. Using normalization condition the restriction $1 = |a|^2 + |b|^2$ can be found.

A point $(a, b) \in \mathbb{C}^2$ fulfill this condition if and only if (iff) it lies on the complex unit circle $S_{\mathbb{C}}^1$. A reasonable parameterization is given by $a = e^{i\delta} \cos\left(\frac{\theta}{2}\right)$, $b = e^{i\delta} \sin\left(\frac{\theta}{2}\right) e^{i\varphi}$, where φ is the polar angle, θ is the azimuthal angle and δ is a global phase. Due to the fact that only scalar products are measured in physics the global phase is of no interest and can be suppressed. This reduction gives now the unitary sphere $S_{\mathbb{R}}^2$ as a new co-domain. It's

elements are called Bloch vectors. The Bloch vectors can be parameterized by $r_z = \cos(\theta)$, $r_x = \sin(\theta)\cos(\varphi)$, $r_y = \sin(\theta)\sin(\varphi)$.

The advantage of the Bloch vector picture will become clear when we discuss operations on the qubit.

If dephasing processes are not taken into consideration all operations O on the qubit are in $SU(2)$. The isomorphism $SU(2) \cong SO(3)/I$ can be found in standard textbook on quantum mechanics. This gives the possibility to see an operation on the qubit as a simple rotation of its Bloch vector in \mathfrak{R}^3 , where the Eigenstates of O are equal to the rotations axis.

The advantage is clear: abstract operations in the special unitary space became now simple rotations in the three dimensional space.

The task in QST is to fully determine the state $|\psi\rangle$, which can be prepared as often as we like. If a measurement is done $|\psi\rangle$ project into a particular state (in our case it would be $|1\rangle\langle 1|$), which is given by the experimental setup. Repeating that measurement several times and building the average, approximates the expectation value

$$p_z = \langle 1|\psi\rangle^2 = \langle 1|(a|0\rangle + b|1\rangle)^2 = |b|^2 = \sin^2\left(\frac{\theta}{2}\right) \stackrel{\text{Trigo.}}{=} \frac{1 - \cos(\theta)}{2} = \frac{1 - r_z}{2},$$

where p_z is the average of the experiments.

This measurement gives a perfect knowledge (only limited by the number of performed measurements) of the r_z component. This results in a total uncertainty of the $x_$ and $y_$ component (see Fig.2.1).

Due to the fact that the state $|\psi\rangle$ can be prepared several times, another measurement series can be done. This time an operation which rotates the Bloch vector around the $y_$ axis by $\frac{\pi}{2}$ is performed before doing the measurements. This means that the Bloch vector $(r_x \ r_y \ r_z)^T$ transforms to $(r_z \ r_y \ -r_x)^T$. If the rotated Bloch vector is now projected into the state $|1\rangle\langle 1|$ and the experiment repeated several times, the expectation value becomes $p_x = \frac{1+r_x}{2}$.

If now rotations around the $x_$ axis were done, it will be possible to determine the r_y component by $p_y = \frac{1-r_y}{2}$.

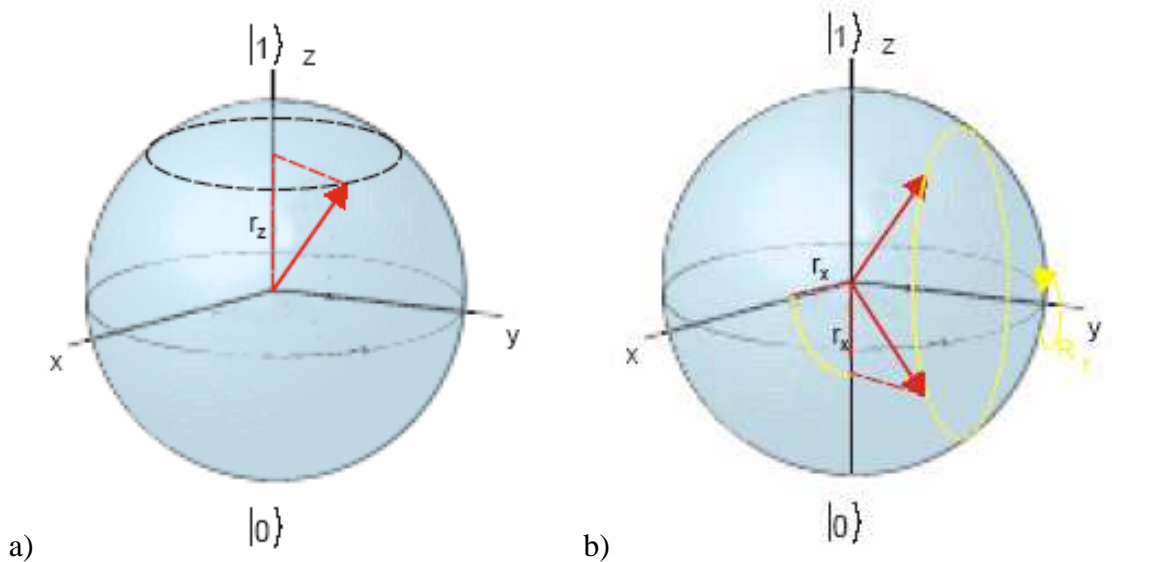


Fig. 2.1 a) Shows the Bloch vectors projection on the $z_$ axis, which is given by the measurement. The uncertainty is pictured by the dashed circle. b) Projection of the Bloch vector on the $z_$ axis (red line) after a $(\pi/2)_y$ pulse (yellow circle) is applied.

2.2 Physical Approach to State Tomography

Doing QST in $S_{\mathfrak{R}}^2$ maybe geometrical simple but it uses difficult mathematics if one wants to do any calculations. However if rotations were done in $SU(2)$, the mathematics will keeps quite simple. For that reason density matrixes and the Von Neumann equation will be introduced.

The concept of density matrixes ρ was introduced by J. von Neumann and is a quite simple description of a quantum mechanical state $|\psi\rangle$. In standard quantum mechanic books [2] one can find the definition of a density matrix by

$$\begin{aligned}\langle A \rangle &= \sum_{i,j} p_{ij} \langle \phi_i | A | \phi_j \rangle = \sum_{i,j,l,k} p_{ij} \langle \phi_i | \phi_l \rangle \langle \phi_l | A | \phi_k \rangle \langle \phi_k | \phi_j \rangle \\ &= \sum_{l,k} \langle \phi_l | A | \phi_k \rangle \langle \phi_k | \sum_{i,j} [p_{ij} | \phi_j \rangle \langle \phi_i |] | \phi_l \rangle = \sum_l \langle \phi_l | A \rho | \phi_l \rangle = Tr(A\rho)\end{aligned}$$

where $\{|\phi_i\rangle\}$, $\{|\phi_j\rangle\}$ are two orthonormal basis's, $\langle A \rangle$ the observable A 's expectation value, $p_{ij} \hat{=} a_i^* a_j$ with a_i defined as $|\psi\rangle = \sum_i a_i |\phi_i\rangle$ and the density matrix is defined as $\rho \hat{=} \sum_{i,j} p_{ij} |\phi_j\rangle \langle \phi_i|$. Further the property $\mathbf{I} = \sum_j |\phi_j\rangle \langle \phi_j|$ was used.

The density matrix ρ has the nice properties:

$$\text{Hermitian: } \rho = \rho^\dagger$$

$$\text{Unity trace: } Tr(\rho) = 1$$

$$|\vec{r}| = \text{Tr}(\rho) \begin{cases} = 1 & : \text{ pure state} \\ < 1 & : \text{ mixed state} \end{cases}$$

The two states of our experiment are label as $|0\rangle \hat{=} \begin{pmatrix} 1 \\ 0 \end{pmatrix}$, $|1\rangle \hat{=} \begin{pmatrix} 0 \\ 1 \end{pmatrix}$. The matrix ρ fulfills the condition of a density matrix iff it can be written as $\rho = \frac{1}{2}(1 + \vec{r} \cdot \vec{\sigma})$. Where \vec{r} is the Bloch vector and $\vec{\sigma} \hat{=} (\sigma_x, \sigma_y, \sigma_z)^T$ is a vector consisting of Pauli spin matrices.

Form the density matrix it is just a small step to the von Neumann equation, which is the analogon to the Schrödinger equation for the wave function. The derivation of the Von Neumann equation is given by [2]

$$\begin{aligned} i\hbar \partial_t \rho &= i\hbar \sum_{i,j} (\partial_t |\varphi_i\rangle) \langle \varphi_j | + |\varphi_i\rangle \langle \partial_t \varphi_j | = \sum_{i,j} \frac{H}{i\hbar} |\varphi_i\rangle \langle \varphi_j | + |\varphi_i\rangle \left(\langle \varphi_j | \left(-\frac{H^\dagger}{i\hbar} \right) \right) \\ &= \sum_{i,j} H |\varphi_i\rangle \langle \varphi_j | + |\varphi_i\rangle \langle \varphi_j | H = [H, \rho] \end{aligned}$$

The von Neumann equation $i\hbar \partial_t \rho = [H, \rho]$ is a system of coupled linear differential equation first order and can be solved analytically for time constant Hamiltonians.

A solution for the Von Neumann equation is $\rho(t) = \text{Exp}\left[-\frac{iH}{\hbar}t\right] \rho(0) \text{Exp}\left[\frac{iH}{\hbar}t\right]$. This can

easily be proved by inserting in the Von Neumann equation and using the commutation relations for $\text{Exp}\left[\frac{iH}{\hbar}t\right]$ and H .

Now the goal is to determine the density matrixes ρ on an arbitrary state, if the Hamiltonian is known. In the experiments H can be written as a function of parameters determined by the experimental setups (see experiments on QST with 3 measurement points).

As discussed before operations $\{O_i\}_3$ were performed on ρ before doing measurements.

The operations $\{O_i\}_3$ are linear independent and in $SU(2)$.

The generators $su(2)$ of $SU(2)$ are given by the Pauli spin matrixes $\sigma_x = \begin{pmatrix} 0 & 1 \\ 1 & 0 \end{pmatrix}$,

$\sigma_y = \begin{pmatrix} 0 & -i \\ i & 0 \end{pmatrix}$ and $\sigma_z = \begin{pmatrix} 1 & 0 \\ 0 & -1 \end{pmatrix}$. This fact allow to write the operations as

$O_j = \text{Exp}[i\vec{r}_j \cdot \vec{\sigma}]$, where $\vec{r}_j \in \mathfrak{R}^3$.

In Chap. *Used Qubit* the Hamiltonian for the Qubit was derived in the previous section and can be written as $H = \frac{\Delta}{2}\sigma_z + \frac{\Omega_x}{2}\sigma_x + \frac{\Omega_y}{2}\sigma_y$. The Hamiltonian is a linear combination of Pauli spin matrixes and is therefore in $su(2)$. The operator $\text{Exp}\left[\frac{iH}{\hbar}t\right]$ is therefore in $SU(2)$. Of course this has to be the case because the Hamiltonian, as it is written down, does not include dephasing processes.

The expectation value by for the projection into the state $|1\rangle\langle 1|$, after the rotation O_j is given by [3]

$$p_j = \text{Tr}(|1\rangle\langle 1|O_j\rho O_j^\dagger) = \text{Tr}(O_j^\dagger|1\rangle\langle 1|O_j\rho)$$

One can easily see that rotating the state $|\psi\rangle$ by $\frac{Ht}{\hbar}$ is equal to rotating the state $|1\rangle\langle 1|$ by $-\frac{Ht}{\hbar}$. It is the same if the projection on three different axis is measured or if the state is rotated by three different rotations before measuring.

A system of linear equations results for an arbitrary density matrix ρ , given rotations $\{O_i\}_3$ and the measured expectations values $\{p_i\}_3$. The solution of the system gives the density matrix ρ .

To clarify the concept the same example as in the section before will be given. We start with an arbitrary density matrix $\rho = \frac{1}{2}(1 + \vec{r} \cdot \vec{\sigma})$ and do QST using rotations $\frac{H_1 t}{\hbar} = \frac{\pi}{4} \sigma_x$, $\frac{H_2 t}{\hbar} = \frac{\pi}{4} \sigma_y$ and $H_3 = 0$. The measurement will do a projection onto the state $|1\rangle\langle 1| = \frac{1 - \sigma_z}{2}$.

The relation $Exp[-i\vec{r} \cdot \vec{\sigma}] = \cos(|\vec{r}|) - i \frac{\vec{r} \cdot \vec{\sigma}}{|\vec{r}|} \sin(|\vec{r}|)$ will be used.

For $\frac{H_1 t}{\hbar} = \frac{\pi}{4} \sigma_x$ can be found

$$\begin{aligned} p_y &= Tr \left(Exp \left[i \frac{\pi}{4} \sigma_x \right] \frac{1 - \sigma_z}{2} Exp \left[-i \frac{\pi}{4} \sigma_x \right] \frac{1}{2} (1 + \vec{r} \cdot \vec{\sigma}) \right) \\ &= Tr \left((1 + i \sigma_x) \frac{1 - \sigma_z}{2} (1 - i \sigma_x) \frac{1}{2} (1 + \vec{r} \cdot \vec{\sigma}) \right) = \frac{1 - r_y}{2} \end{aligned}$$

For $\frac{H_2 t}{\hbar} = \frac{\pi}{4} \sigma_y$ can be found

$$\begin{aligned} p_x &= \text{Tr} \left(\text{Exp} \left[i \frac{\pi}{4} \sigma_y \right] \frac{1 - \sigma_z}{2} \text{Exp} \left[-i \frac{\pi}{4} \sigma_y \right] \frac{1}{2} (1 + \vec{r} \cdot \vec{\sigma}) \right) \\ &= \text{Tr} \left((1 + i \sigma_y) \frac{1 - \sigma_z}{2} (1 - i \sigma_y) \frac{1}{2} (1 + \vec{r} \cdot \vec{\sigma}) \right) = \frac{1 + r_x}{2} \end{aligned}$$

For $\frac{H_3 t}{\hbar} = 0$ can be found

$$p_y = \text{Tr} \left(\frac{1 - \sigma_z}{2} \frac{1}{2} (1 + \vec{r} \cdot \vec{\sigma}) \right) = \frac{1 + r_z}{2}$$

Of course this is the same result as found previously.

3 Experimental setups

Here we will discuss how the theoretical ideas from Chap *Used Qubit* are implemented in the experimental setup. This will be of some interest when we address some experimental properties as the mixers nonlinearity and the chosen pulse sequences.

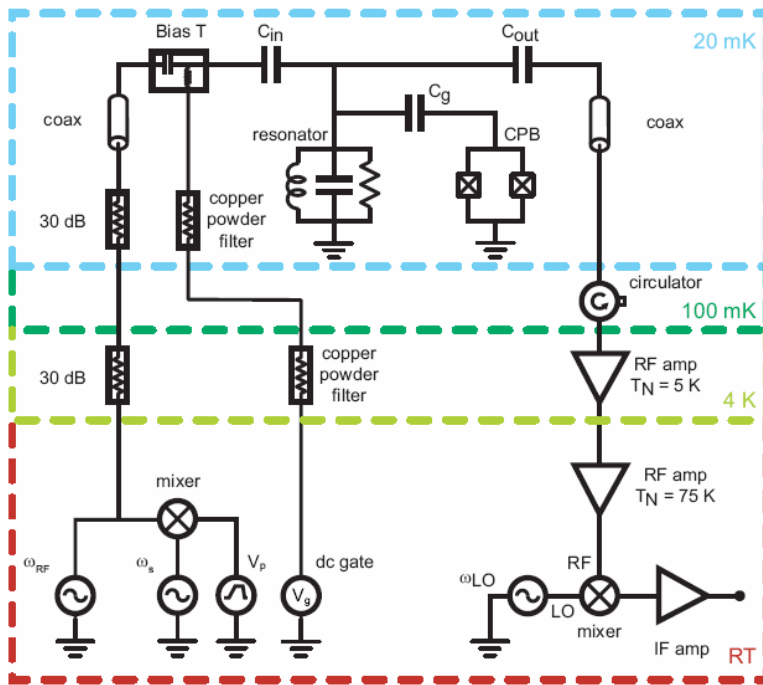


Fig. 3.1 Schematically picture of the used circuit. The Cooper pair box (CPB) is attached to the gate C_g . The cavity is defined by the capacities C_{in} and C_{out} . This can also be found in Fig. . The microwave generators are set in the picture's lower left corner. The analyzer is placed in the picture's lower right corner.

The operations on the Qubit are performed by microwaves at frequency ω_s , created by a microwave generator.

The used microwaves for Qubit operations had either 6 dBm or 13 dBm power. This high power is needed because the system is strongly detuned (see chapter *coupling to cavity*).

The operation is given by the microwave pulse's amplitude integrated over the time and the pulse's phase, e.g. microwave pulses for rotation around the x axis are 90° phase shifted to pulses for rotation around the y axis.

The pulse shape is controlled on a 1 ns time scale by two properties a mixer and the possibility to turn the microwave generator on/of. As we will see in the discussion on the mixer's property it is crucial to turn the microwave generator off if no operation pulse should be performed.

The mixer's input is a microwave pulse with 6 dBm or 13 dBm power as well as two dc voltages $V_p = (V_x, V_y)$. The mixer's output is a microwave pulse with new phase and new amplitude. The output microwave's phase φ is given by $\tan \varphi = V_y/V_x$ and the output pulse's amplitude by $P_s^{mix} \propto \sqrt{V_x^2 + V_y^2}$. In Chap. *Experiments* it will be seen that the mixer behaves not linear and a calibration has to be done.

To set the gate charge n_g on an odd electron number integer a dc gate voltage was applied.

The microwaves as well as the gate voltage undergo two filters, at 4 K and 20 mK , to suppress thermal noise.

The cavity, with a frequency ω_{RF} , is a coplanar waveguide. The cavity's "mirrors" are two capacities C_{in} and C_{out} , which determine the transmissions rate κ . This is similar to a coax cable with bad contact where the signal is reflected.

For readout another microwave generator emits microwaves at the resonator frequency $\omega_{RF} = 5.42573 \text{ GHz}$. To justify the assumption (small photon number n) made in Chap. *Used Qubit* the RF power was in the range of -31 to -26 *dBm* (10 to 30 photons in the cavity).

In the most experiment RF was pulsed, which means that the RF microwave generator was only turned on during the measurement process.

To ensure that no signal (especially thermal noise) accesses the cavity through the readout line a circulator is connected after the cavity at 100 *mK* and 20 *mK*. A signal can only pass a circulator in one direction.

The signal for readout passes then a chain of amplifier at 4 *K* and room temperature.

The signal has too high frequency to be analyzed, therefore it is mixed down with a LO generator to decrease the frequency by a beat process (10 *MHz*).

The signal is then, before digital registered, again amplified.

4 Experiments

The goal in the performed experiments was to prove that QST is possible and to develop a method that can be applied later in different experiments. For that reason the experiments were divided in three tasks.

In the first section the aim was to demonstrate that QST for the used system works in principle.

For totally four different prepared states the response was measured as a function of 1681 (=41x41) different rotations. This allowed to map a two dimensional plot (2DP) for the response of the Qubit as a function of the applied microwave pulses.

In a first part the tomography pulses were aligned in serial.

In a second part measurements have been done on parallel pulse sequences.

The method used in the first section is not appropriated to determine a state in a reasonable time. Therefore a method was developed which only uses three operations to determine the complete quantum state. Three operations are the minimal number needed to describe an arbitrary quantum state. The analysis process was done in such a way that the only restriction to the operations is that they are linear independent.

In the third section QST, using three operators, was performed in a Ramsey experiment. The Bloch vector rotates around the z -axis with the detuning frequency. Due to dephasing process the Bloch vector shrinks monotonously. The experimental data for that experiment were quite bad, but it still shows that the experiment works in principle.

All Mathematica programs that have been used for analysis can be found on the QUDEV server `Q:\USERS\Peter Maurer\Tomography\`.

4.1 Dephasing processes

From experiments in a second experiment [4] it is known that the Qubit has a dephasing time $T_2 \approx 650 \text{ ns}$ and $T_2^* \approx 2 \text{ } \mu\text{s}$. The relaxations time $T_1 \approx (4-6) \text{ } \mu\text{s}$ (with (30-10) photons in the cavity).

The tomography pulses are on a time scale of 10 ns to 20 ns. This is much smaller than the dephasing time. Simulations show that dephasing can be neglected (Fig. 4.1).

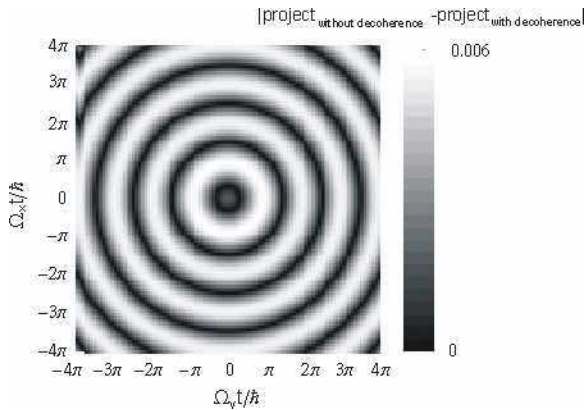


Fig. 4.1 Shows the absolute value of the difference for the response for a simulation with dephasing and without dephasing starting in the ground state. One can see that the difference is smaller than 0.6%.

Therefore and for the fact that the system of equation, to calibrate the tomography pulse would become very complicated, the effect of dephasing during QST will be neglected in the whole experiments.

4.2 Serial pulse sequence

Here QST in serial sequence have been done because it was simple and proofs that QST works in principle.

To our knowledge this has never been published so far. However the serial sequence does not have any advantage compared to parallel sequence (which is probably the reason why nobody mentioned it).

4.2.1 Simulation

To perform operations on the Qubit two microwave pulses were applied in serial. In the experiment the pulses amplitude was kept constant, only the pulses length was varied. Further the assumption was made that the Eigen vectors of the operations are perpendicular to each other and that dephasing processes can be neglected (operations pulses $t < 20$ ns).

This procedure is given by the two Hamiltonians

$$H_x = \frac{\Delta}{2}\sigma_z + \frac{\Omega_x}{2}\sigma_x \text{ and } H_y = \frac{\Delta}{2}\sigma_z + \frac{\Omega_y}{2}\sigma_y$$

as discussed previously.

The formula derived in Chap. *QST* can be used to calculate the response

$$p_j = \text{Tr} \left(\text{Exp} \left[i \frac{H_y^j}{\hbar} t_y^j \right] \text{Exp} \left[i \frac{H_x^j}{\hbar} t_x^j \right] \frac{1 - \sigma_z}{2} \text{Exp} \left[-i \frac{H_x^j}{\hbar} t_x^j \right] \text{Exp} \left[-i \frac{H_y^j}{\hbar} t_y^j \right] \rho \right).$$

These calculations were performed for the states $\rho = |0\rangle$, $|1\rangle$, $(|0\rangle + |1\rangle)/\sqrt{2}$ and $(|0\rangle + i|1\rangle)/\sqrt{2}$.

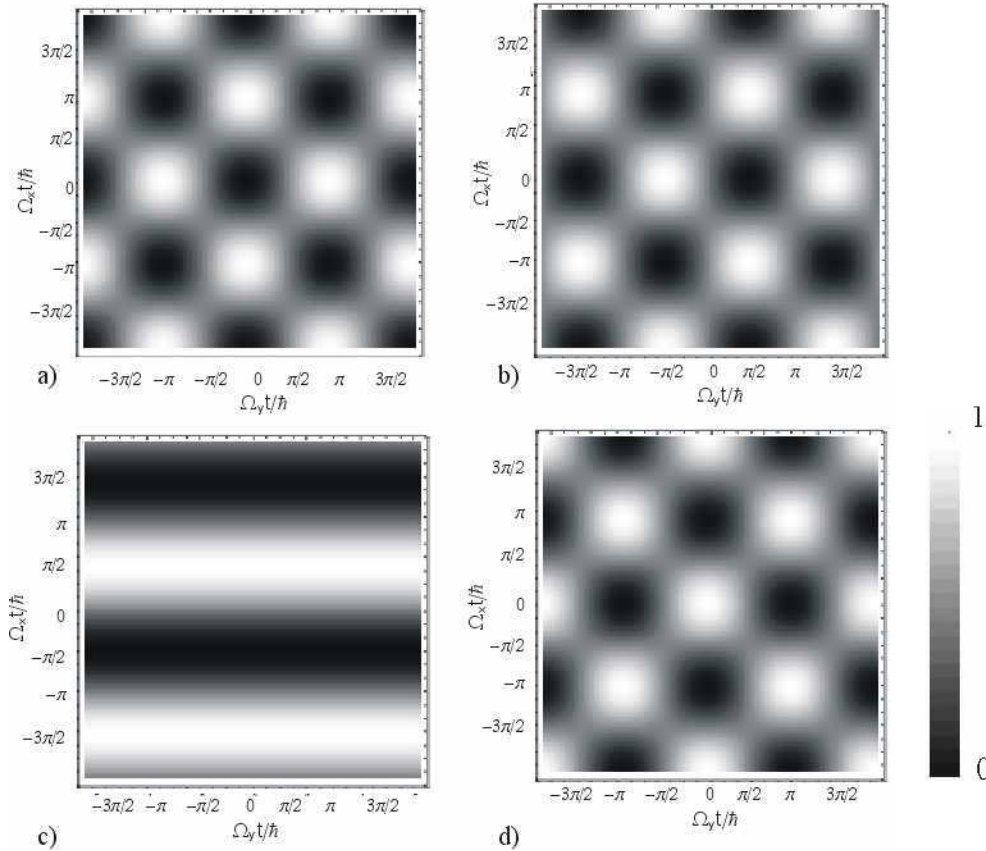


Fig. 4.2 Shows simulation of the response for a) the ground state $|0\rangle$, b) the superposed state $(|0\rangle + |1\rangle)/\sqrt{2}$, c) the superposed state $(|0\rangle + i|1\rangle)/\sqrt{2}$ and d) the excited state $|1\rangle$.

The checkerboard pattern for the cases $\rho = |0\rangle, |1\rangle$ and $(|0\rangle + |1\rangle)/\sqrt{2}$ can be easily verified by using the Bloch vector picture.

In the other case $\rho = (|0\rangle + i|1\rangle)/\sqrt{2}$ is an Eigen state of the operation H_y^j . Therefore only the rotations performed by H_x^j change ρ . This yields to the stripe pattern above.

4.2.2 Results

The checkerboard pattern expected from the simulation was reproduced by the measurement (Fig. 4.3). This demonstrates that state tomography works in principle.

The contrast variation in the pattern can be explained by the fact that the measurement was mapped with constant $\Omega_x t/\hbar$. Between different measured sequence files fluctuations in n_g may occur, which results in change of contrast.

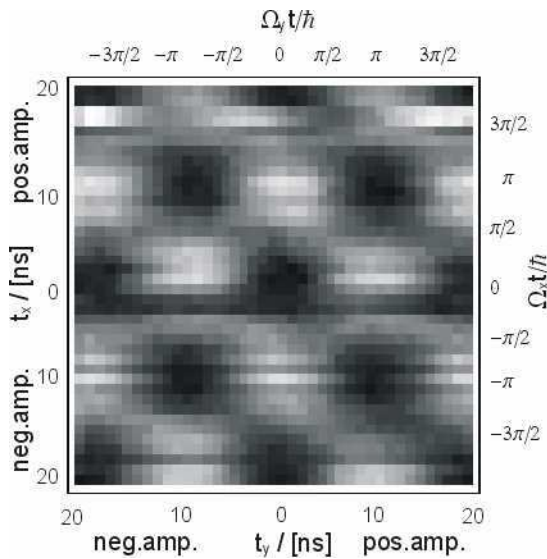


Fig. 4.3 Shows *QST* on the ground state. The scaling for the response is in arbitrary units.

The setups for the measurements were:

For the measurement the operations pulses were applied in serial with fix amplitude. The maximal pulse length was 20 ns for each pulse. The spec. power was 6 dBm at 400 mV for rotations clockwise and -400 mV for rotations counterclockwise. A possible non linearity of the microwave pulse mixer was not taken into consideration. The spectroscopy frequency was adjusted at 3.702 GHz .

The RF power was -33 dBm .

100 ns spare time were inserted between the pulse and the recorded measurement. This is done to ensure that the measured signal is not affected by the operations pulse.

The microwave generator can be turned off/on with a response time of 75 ns and the power raises over 2 ns . Therefore the backup pulse starts 77 ns earlier and is enlarged by 2 ns .

A schematically plot of the pulse sequence is given in Fig. 4.4.

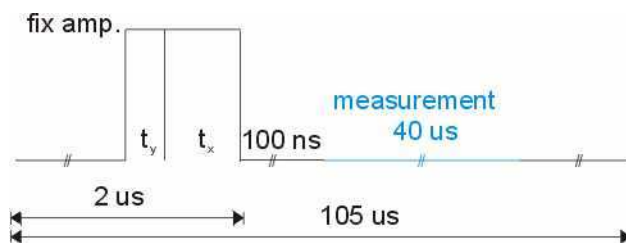


Fig. 4.4 Shows the parallel pulse sequence. The pulses have fix amplitude but vary in their length.

4.2.3 Response

As mentioned in Chap. *The used Qubit* the response is Poisson distributed.

For the resonators response a differential equation can be found. This was implemented in a Mathematica by A. Blais.

As a measure for the projection of the Qubit into the state $|1\rangle\langle 1|$ the normalized scalar product between the measured response $\tilde{r}(t_n)$ and the theoretical response $r(t_n)$ can be used

$$p_j = \frac{\sum_{t_n \in T} (\tilde{r}(t_n) - \tilde{r}_{Base}) r(t_n)}{\sum_{t_n \in T} r^2(t_n)}.$$

Where T is the set of the measured times and \tilde{r}_{Base} is the offset determined by taking the average for responses at times larger than 37 us (one can assume that Qubit is in its ground state). This is justified by the assumption that T_1 is smaller then 6 us .

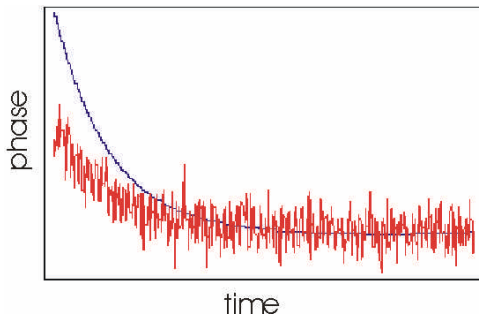


Fig. 4.5 Shows an example for the response. The visibility is lower then 1, because the measured response is lower than the expected one. The normalized scalar product between the experiment (red) and the theory (blue) is a measure for the population.

4.2.4 Pattern files

The mixer's input dc voltages V_X and V_Y are each controlled a 10 bit canals. The measurement program interpolated and indices automatically 1024 equidistant voltages between V_X^{\min} and V_X^{\max} , V_Y^{\min} and V_Y^{\max} respectively.

The bit pattern for the voltages V_X and V_Y are given by the pattern files in Fig. 4.6.

This pattern files are connected in one sequence file. Therefore in a sequence file the x_pulse length varies form 0 to 20 ns for -400 mV and 400 mV amplitude where the y pulse length remains constant.

For averaging each sequence file was measured ten thousand times.

After the measurement, it was manually verified if the signal has been lost during the measurement process, due to shifts in n_g . If that was the case the measurement was repeated. Otherwise the next sequence file with another y_pulse length was loaded.

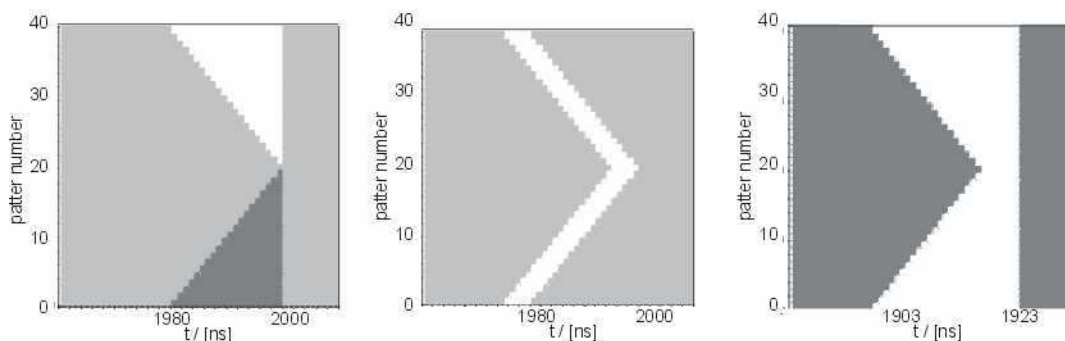


Fig. 4.6 Shows the used pattern files. The first two determine the operation pulses' amplitude (black -400 mV, grey 0, white 400 mV) and the pulse length. The third turns the microwave generator one/off.

4.3 Parallel pulse sequence

A more standard used procedure for doing QST is in applying x and y pulses in parallel.

4.3.1 Simulation

The same assumptions as in the simulation on serial pulse sequences (no dephasing and orthogonal operations) were made.

The Hamiltonian is then given by

$$H = \frac{\Delta}{2} \sigma_z + \frac{\Omega_x}{2} \sigma_x + \frac{\Omega_y}{2} \sigma_y.$$

The response is determined by

$$p_j = \text{Tr} \left(\text{Exp} \left[i \frac{H^j}{\hbar} t^j \right] \frac{1 - \sigma_z}{2} \text{Exp} \left[-i \frac{H^j}{\hbar} t^j \right] \rho \right).$$

Due to the non commutation relation of σ_x and σ_y it can be easily seen that serial and parallel pulse sequences are different.

These calculations were performed for the states $\rho = |0\rangle$, $|1\rangle$, $(|0\rangle + |1\rangle)/\sqrt{2}$ and $(|0\rangle + i|1\rangle)/\sqrt{2}$.

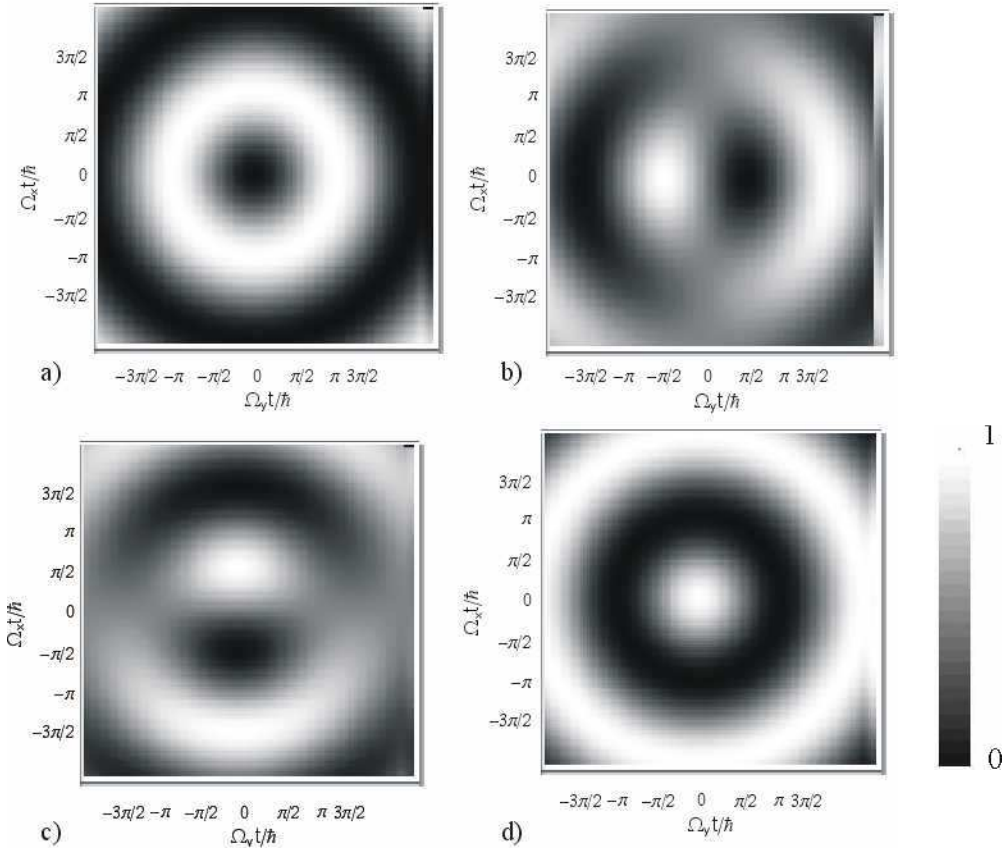


Fig. 4.7 Shows simulation of the response for a) the ground state $|0\rangle$, b) the superposed state $(|0\rangle + |1\rangle)/\sqrt{2}$, c) the superposed state $(|0\rangle + i|1\rangle)/\sqrt{2}$ and d) the excited state $|1\rangle$.

The central symmetry for $\rho = |0\rangle$ and $|1\rangle$ can be verified by arguing that the measurement setup defines the z_axis. But the system has still rotation symmetry and the result only depends on the magnitude of the rotation and not of the phase.

For the example the prepared states $\rho = (|0\rangle + |1\rangle)/\sqrt{2}$ and $(|0\rangle + i|1\rangle)/\sqrt{2}$ have not the symmetry mentioned before.

4.3.2 Results

If a calibration for the mixer (see calibration) is used the measurements are in good agreement with the simulation (Fig. 4.8). Again change in the contrast between different measurements yield from fluctuations in n_g .

As discussed previously the ground and excited state have rotations symmetry around the z axis. Therefore the projection on the z axis depends only on the rotation's angle and not on the rotation's axis orientation in the x-y plane. This can be seen in both cases.

The rotation's symmetry around the z axis is broken for the superposed state. Therefore the response is not rotations symmetric. The superposed states $(|0\rangle + |1\rangle)/\sqrt{2}$ (Fig. 4.8 c) and $(|0\rangle + i|1\rangle)/\sqrt{2}$ (Fig. 4.8 b) are eigenstates for all rotations around the x axis, for all rotations around the y axis respectively. This can be seen by the line of constant response intersecting the plot.

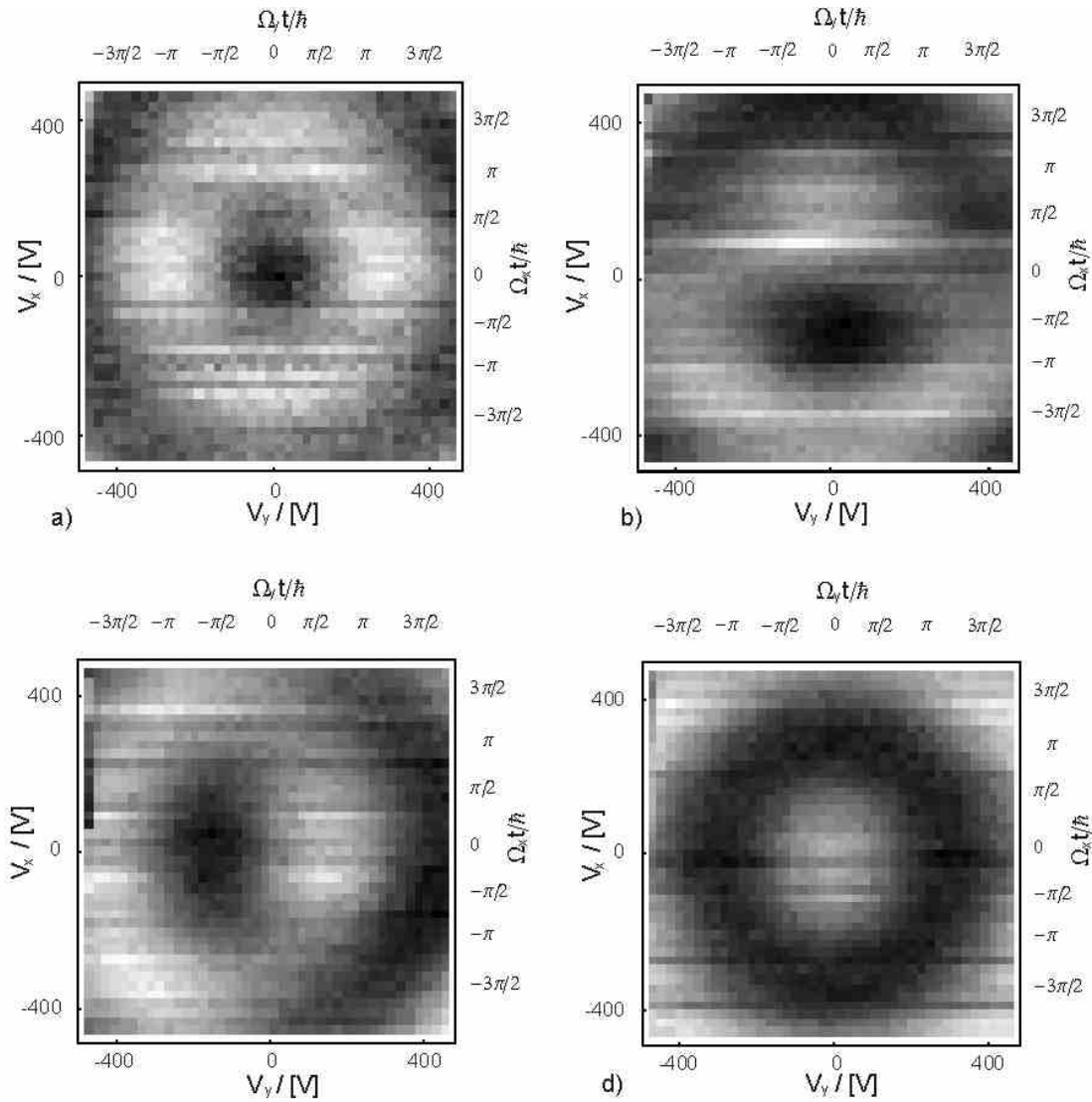


Fig. 4.8 Shows measurement of the response for a) the ground state $|0\rangle$, b) the superposed state $(|0\rangle + i|1\rangle)/\sqrt{2}$, c) the superposed state $(|0\rangle + |1\rangle)/\sqrt{2}$ and d) the excited state $|1\rangle$. This is in good contradiction with the simulations. The scaling for the response is in arbitrary units.

The setups for the measurements were:

The operations pulses were applied in parallel with varying amplitude. The pulse length was 10 ns. The spec. power was 13 dBm with mixer voltages varying from -400 mV to 400 mV. The spectroscopy frequency was adjusted at 3.704 GHz.

The RF power was -26 dBm (30 photons in the cavity).

Between the pulse and the measurement 100 ns spare time were inserted.

The measurements were performed in pulsed mode.

The other settings were the same as before.

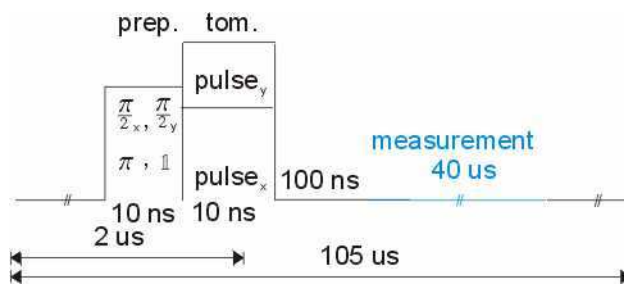


Fig. 4.9 Shows the parallel pulse sequence. The pulses have fix length but vary in their amplitude. The first pulse prepare the state and the second is for tomography.

4.3.3 Calibration

Unfortunately the mixer was used outside of its specific fabrication's range. Therefore the output is not linear to the input voltage. This means that the properties $\tan \varphi = V_Y / V_X$ and $P_S^{mix} \propto \sqrt{V_X^2 + V_Y^2}$ given in Chap. *experimental setups* do not hold exactly.

To record a calibration curve the mixer's output power was measured in function of the voltages V_X and V_Y for 6 dBm and 13 dBm power (Fig. 4.10).

However the used analyzer only allowed determining the power, to measure the microwaves phase a *vector analyzer* would need to be used.

Knowing the phase is crucial for calibration. Because the phase could not be measured the assumed was made that the phase does not change ($V_y/V_x \approx const.$).

This assumption allows to calculate the voltage which has to be applied to receive the desired output power under the condition $\tan \varphi = V_y/V_x$.

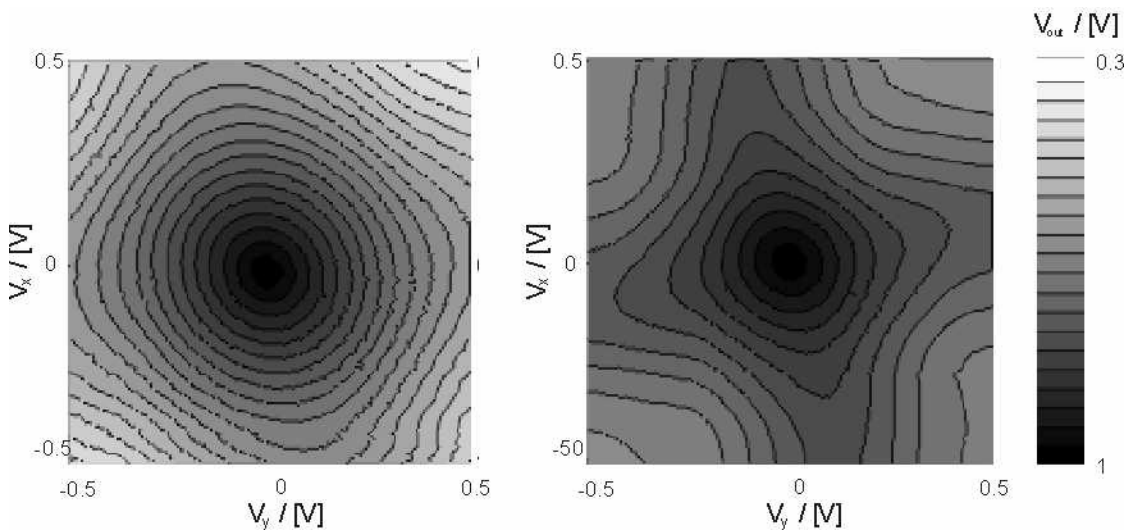


Fig. 4.10 Shows the mixer's output for 13 dBm input microwave power left and 6 dBm right. In an ideal case this would be equidistant concentric circles.

The advantage of the calibration can immediately be seen in Fig. 4.11 where the same measurement was done without and with calibration. The calibrations curve's shape can be recognized in the shape of the QST measurement.

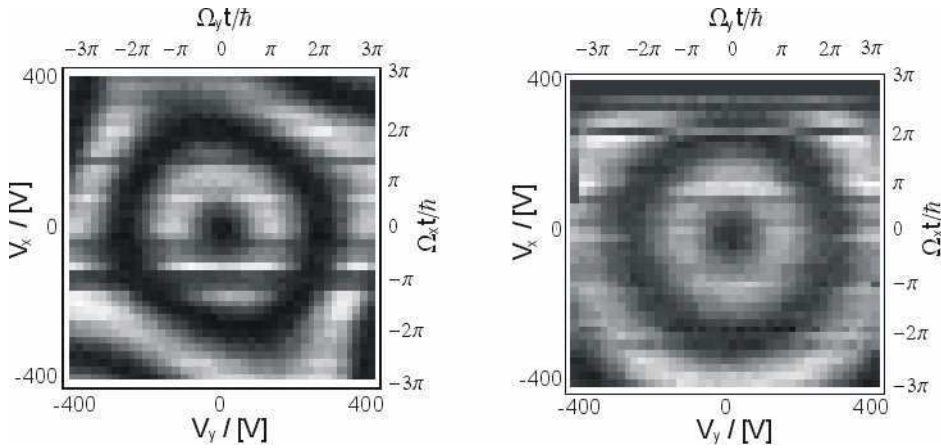


Fig. 4.11 Shows the same measurement without and with calibration left/right. The left measurement has the same asymmetry as the mixer's output in Fig. 4.10. The right one demonstrates the ability to get rid of this effect. The scaling for the response is in arbitrary units.

4.3.4 Pattern files

The bit pattern for the voltages V_x and V_y are given by the pattern files in Fig. 4.12.

This pattern files are connected in one sequence file. Therefore in a sequence file the `x_pulse` length remains constant where the amplitude varies for -400 mV to 400 mV . The `y_pulse`'s amplitude stays constant.

Each sequence file was measured ten thousand times and then averaged.

The decision process on using the measurement was the same as in the measurements on serial pulses.

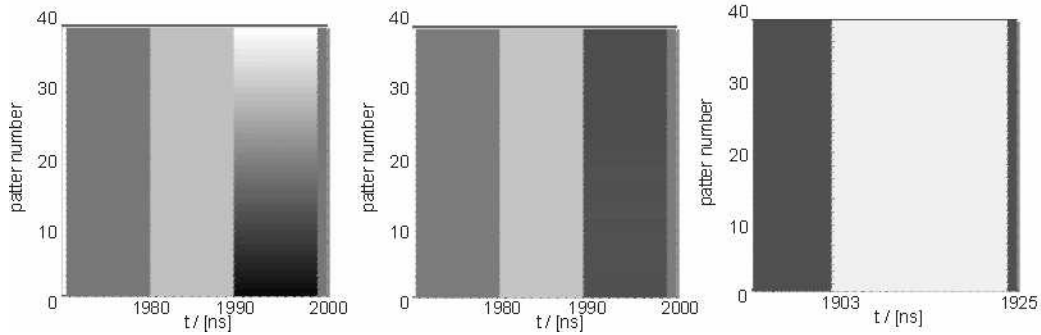


Fig. 4.12 Shows the used pattern files. The first two determine the operation pulses' amplitude. In the pattern file the first pulse is to prepare the state and the second for tomography (one tomography pulse varies from negative to positive where the other remains the same) The pulse length is constant 10 ns. The third turns the microwave generator one.

4.4 Quantum state tomography using three operations

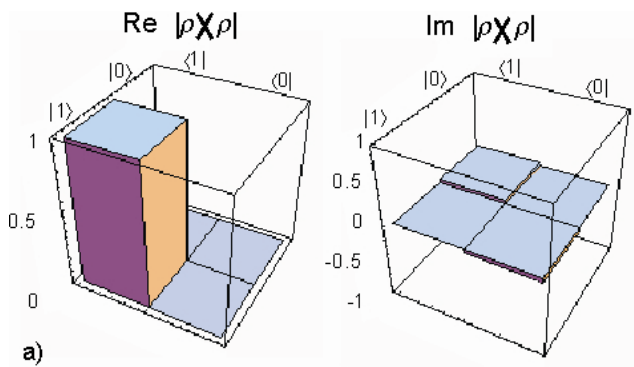
For QST's application it is unsatisfying to determine for each state a whole 2 dimensional plot. As shown in Chap. *Quantum state tomography* indeed only three operations are necessary. The QST method derived here will be able to reconstruct a quantum state even if the used operations are completely unknown.

The only restriction is that the operations are linear independent. As discussed later the measurements will be more accurate if the operations are close to orthogonal.

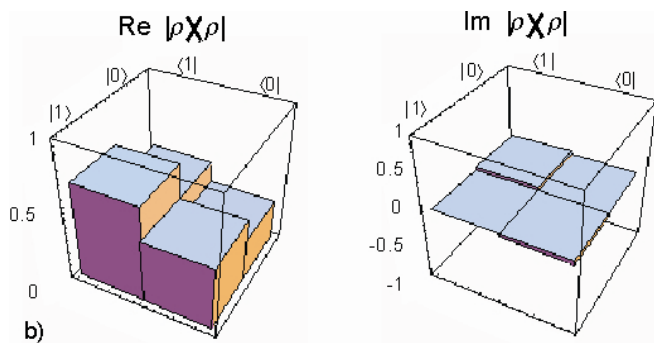
4.4.1 Results

To demonstrate that this simplified method for QST works the states $|1\rangle$, $(|0\rangle + |1\rangle)/\sqrt{2}$ and $(|0\rangle + i|1\rangle)/\sqrt{2}$ were be prepared and determined.

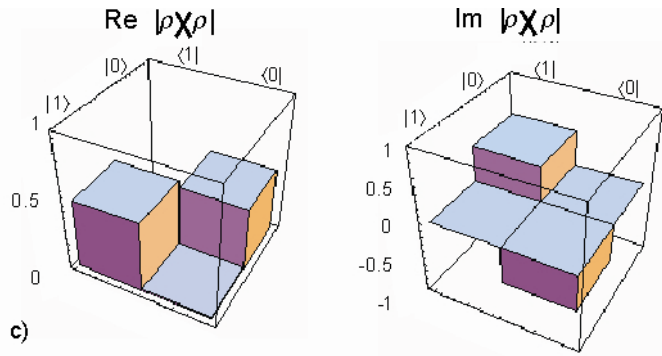
The states were prepared with the same imperfect $\pi/2$ pulses as used for the QST. This does not matter because it will be taken into account that the pulses are not perfect.



$$\rho = \begin{pmatrix} 0.99 \pm 0.03 & (-0.04 \pm 0.08) \pm i(0.04i \pm 0.14) \\ (-0.04 \pm 0.08) \pm i(0.04i \pm 0.14) & 0 \pm 0.03 \end{pmatrix}$$



$$\rho = \begin{pmatrix} 0.736 \pm 0.004 & (0.44 \pm 0.03) + i(0.02 \pm 0.03) \\ (0.44 \pm 0.03) + i(0.02 \pm 0.03) & 0.263 \pm 0.004 \end{pmatrix}$$



$$\rho = \begin{pmatrix} 0.5224 \pm 0.0007 & (-0.11 \pm 0.05) + i(0.49 \pm 0.08) \\ (-0.11 \pm 0.05) + i(0.49 \pm 0.08) & 0.4775 \pm 0.0007 \end{pmatrix}$$

Fig. 4.13 Shows the measured density matrixes by using QST for three different prepared states. State a) is prepared in the excited state $|1\rangle$. State b) is not exactly in the desired superposed state $|0\rangle + |1\rangle$ (probable the amplitude for preparation was little to high). The prepared state c) is very close to the desired state $|0\rangle + i|1\rangle$. The error bars give the standard deviation.

One can immediately recognize the different states. The $(\pi/2)_x$ pulses vary significantly from the desired value. This justifies why the operations pulse have to be treated as unknown.

It is worth to mention that the accuracy in the diagonal element is much smaller than in the off diagonal element. The explanation is that the diagonal element is measured without applying any pulses where the off diagonal elements need tomography pulses to be determined. Since the tomography pulses have to be measured first and they have a extra accuracy.

However it makes sense to measure the tomography pulse firsts because it is convenient not to adjust always the $\pi/2$ pulses before measuring.

Another argument is that otherwise the error could not be calculated.

The error bars in the density matrix marks the standard deviation.

Rabi oscillation measurements are always attached to QST measurements (see *Visibility*).

If the assumption is made that the measurement for the Rabi points have the same accuracy as the QST measurements (this makes sense because there is no different in the process), the measurements from the Rabi oscillation can be used to calculate the standard deviation for the QST process.

$$\text{var} = \frac{1}{N} \sum_{j=0}^N (p_j - p_j^{\text{theory}})^2$$

Where var is the variance, p_j is the projection on the excited state and p_j^{theory} is the theoretical projection for a Rabi experiment (see *Visibility*).

This variance gives the accuracy for the measurement process. It can be used to determine the accuracy in the operation pulses and to find the error in the QST process.

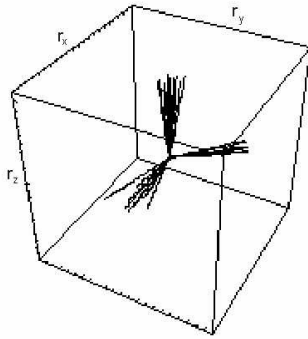
To calculate the accuracy in the operation pulses an analytical error calculation was made using the variance, estimated above. Unfortunately the analysis also involves numerical solving of an equation system. At this point the error propagation was estimated by solving the equation system with the lowest and highest possible values.

In all other cases the error propagation was treated analytically.

The accuracy can be tested in another way by repeating the measurement several times.

The results are plotted in Fig. 4.14 as Bloch vectors.

This allows calculating the standard deviation in the polar and azimuthal angle.



$$\begin{aligned}
 s(\theta_{|1\rangle}) &= 0.001 \\
 s(\theta_{|0\rangle+|1\rangle}) &= 0.011, \quad s(\varphi_{|0\rangle+|1\rangle}) = 0.015 \\
 s(\theta_{|0\rangle+i|1\rangle}) &= 0.35, \quad s(\varphi_{|0\rangle+i|1\rangle}) = 0.06
 \end{aligned}$$

Fig. 4.14 Shows states measured by QST. One can see that they are spread. The standard deviations are calculated for azimuthal and polar angles.

The accuracy is here less than 10° . This is consistent with the calculations done above.

The setups for the measurements were:

For the measurement the operations pulses were applied in parallel. The amplitude of the $\pi/2$ pulses was adjusted. These pulses were not exact $\pi/2$. The maximal pulse length was 10 ns for each pulse. The spec. power was 13 dBm at a mixer voltage of 450 mV. The spectroscopy frequency was adjusted at 3.709 GHz.

The RF power was -26 dBm (30 photons in the cavity).

Between the pulse and the measurement were 100 ns spare time inserted.

A schematically plot of the pulse sequence is given in Fig. 4.15.

The underground was determined by projecting $|0\rangle$ on the state $|1\rangle\langle 1|$ and then averaging the response.

The excited state $|1\rangle$ was prepared by a 10 ns pulse with $(0.23, -0.01)$ V amplitude. The superposed state $(|0\rangle + |1\rangle)/\sqrt{2}$ was generated by a 10 ns pulse with $(0.13, -0.01)$ V amplitude. The other superposed state $(|0\rangle + i|1\rangle)/\sqrt{2}$ was prepared by a 10 ns pulse with $(-0.02, 0.15)$ V amplitude.

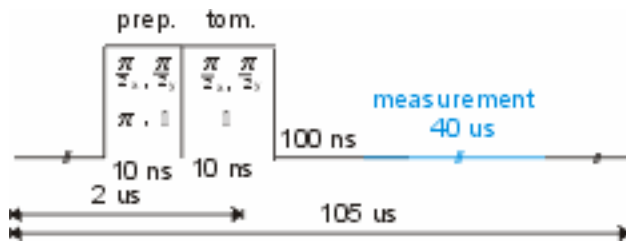


Fig. 4.15 Shows the parallel pulse sequence. The pulses have fix length but vary in their amplitude. The first pulse prepare the state and the second is for tomography.

4.4.2 Calibrations

A proper calibration is crucial for state tomography.

A calibration for the tomography pulses is implemented into the analysis process and allows also doing QST if the tomography pulses are not perpendicular and not $\pi/2$.

As important as the knowledge of the tomography pulses is the knowledge of the visibility. If the visibility is not corrected one would guess a wrong projection on the z -axis.

4.4.2.1 Calibrating the tomography pulses

As tomography pulses the identity, a $(\pi/2)_x$ -pulse and a $(\pi/2)_y$ -pulse were used.

As showed by the experiment above (Fig. 4.13) the $\pi/2$ pulses are not perfect. We also expect that the V_p voltage used to create a $\pi/2$ pulse may change over time.

These make it necessary to find a process to do QST with unknown pulses. This is done by calibrating the tomography pulses during the analysis process.

For simplicity we will first discuss the calibration in the Bloch vector picture and then use the density matrixes for calculations.

We assume that the identity is perfect and can be realized easily by not applying any pulse. This defines the z -axis.

Now it is known that the $(\pi/2)_x$ -pulse is imperfect. That means the actual orientation of the rotation axis and amplitude is not known exactly. However the polar angle, does only give us a global phase, which is of no interest. If the $(\pi/2)_x$ -pulse is applied on the

ground state and then projected on the $|1\rangle\langle 1|$ state, the azimuthal angle can be calculated immediately. The $(\pi/2)_x$ pulse is now known.

For the $(\pi/2)_y$ pulse the situation is trickier, because the polar phase is now also of relevance. This time two parameters are to measure, the azimuthal and the polar angle. The azimuthal angle can be determined by the same way as before. The polar angle can be measured by applying a $(\pi/2)_y$ pulse on the ground state followed by a $(\pi/2)_x$ pulse and then projected on the $|1\rangle\langle 1|$ state. The $(\pi/2)_y$ pulse is now also known.

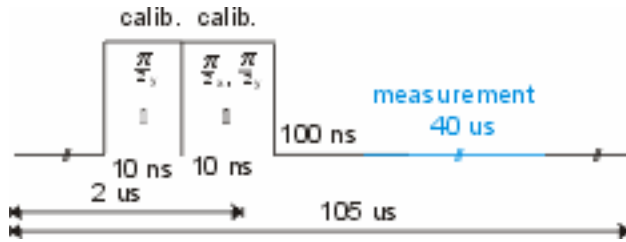


Fig. 4.16 Shows the parallel pulse sequence. The pulses have fix length but vary in their amplitude. Both pulses are for calibration.

Using density matrixes the problem can be reformulated as determining the Hamiltonians $\frac{H_x t}{\hbar} = \frac{\Omega_x t}{2\hbar} \sigma_x$ and $\frac{H_y t}{\hbar} = \frac{\Omega_x t}{2\hbar} \sigma_x + \frac{\Omega_y t}{2\hbar} \sigma_y$. In the first Hamiltonian the part $\frac{\Omega_y t}{2\hbar} \sigma_y$ is missing because the global phase is not of interest.

Applying the x_pulse followed by the measurement gives

$$P_x^{calibr.} = Tr \left(Exp \left[i \frac{H_x t}{2\hbar} \right] |1\rangle\langle 1| Exp \left[-i \frac{H_x t}{2\hbar} \right] |0\rangle\langle 0| \right).$$

$p_x^{calibr.}$ is given by the measurement. This is an equation for $\frac{\Omega_x^y t}{2\hbar}$ which can be solved analytically.

The other Hamiltonian consists of two unknown components. Therefore two equations have to be found.

The first measurement is analogue to the one before

$$(I) \quad p_y^{calibr.} = Tr \left(Exp \left[i \frac{H_y t}{2\hbar} \right] |1\rangle\langle 1| Exp \left[-i \frac{H_y t}{2\hbar} \right] |0\rangle\langle 0| \right)$$

and the second is given by

$$(II) \quad p_{yx}^{calibr.} = Tr \left(Exp \left[i \frac{H_y t}{2\hbar} \right] Exp \left[i \frac{H_x t}{2\hbar} \right] |1\rangle\langle 1| Exp \left[-i \frac{H_x t}{2\hbar} \right] Exp \left[-i \frac{H_y t}{2\hbar} \right] |0\rangle\langle 0| \right)$$

The equations system (I, II) can be solved.

(I) can be rephrase as function of $\frac{\Omega_y^y t}{2\hbar}$ and insert it in (II). This must then be solved numerically.

Now the problem of not orthogonal pulses has been eliminated.

4.4.4 Visibility

The visibility has a direct influence on the result in QST. If the visibility was not corrected, the calibrations on the pulse as well as the QST it self would be completely wrong. If the visibility is low, one would calculate that the projection is small and calculate a wrong state.

Therefore the visibility is corrected by performing Rabi oscillations. Then a cosine function is fitted to the data. The Rabi points are then multiplied by a constant so that the amplitude becomes one (Fig. 4.17).

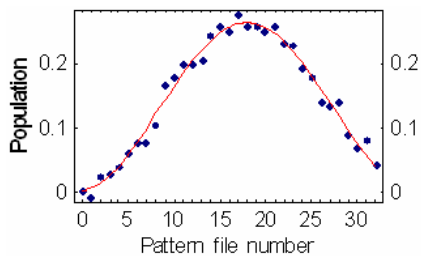


Fig. 4.17 Shows the measured population in a experiment. The red line is a fitted cosine. This is used to estimate the error bar as well as to determine the visibility.

4.4.5 Pattern files

A sequence file consists of three parts first the four calibrations pulses, second three tomography pulses and thirdly thirty pulses for Rabi oscillation.

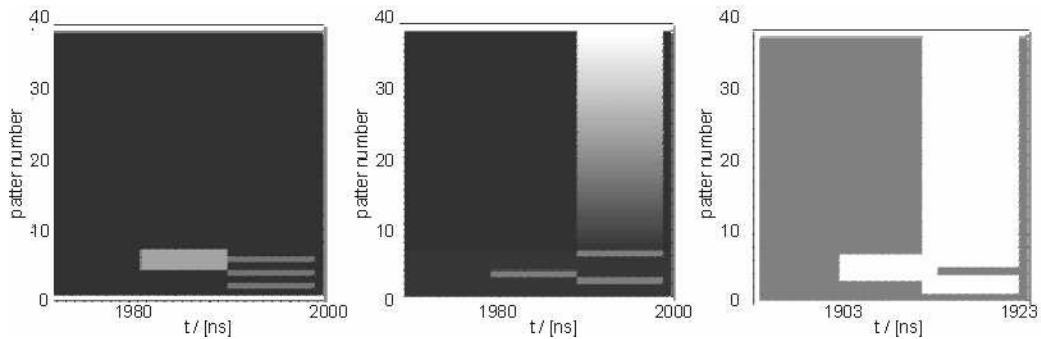


Fig. 4.18 Shows the used pattern files. The first two determine the operation pulses' amplitude. The pattern file has four pulse for calibration, three for tomography and thirty for Rabi. The pulse length is constant 10 ns. The third turns the microwave generator one/off.

This pattern files are in one sequence file.

The first pattern is to determine the underground, the next three are for the pulse calibration and the following three are for tomography.

The last thirty are to perform Rabi oscillations. Therefore in a sequence file for Rabi oscillations the x_pulse length remains constant where the amplitude varies for -0.02 mV to 450 mV .

Each sequence file was measured ten thousand times and then averaged.

Again Peter Leek's program was used to adjust n_g .

The decision process on using the measurement was the same as in the measurements on serial pulses.

4.5 Ramsey

To show an application of QST Ramsey experiments were performed. A similar experiment can be found in [3] with a much better accuracy. Probably this group invested more time in doing the experiment and they created the pulse with a different microwave generator.

An expanded treatment of Ramsey experiment can be found in Lars' Semesterarbeit [4].

In this experiment we apply first a preparations pulse, which brings the Qubit in the superposed state $(|0\rangle + |1\rangle)/\sqrt{2}$. Then QST is done after a variable time between the preparations pulse and the tomography. Due to the detuning the Bloch vector will process around the z -axis. This can be pictured by QST.

4.5.1 Results

Unfortunately the Qubit was jumping very much that day and only a half experiment could be performed. However this experiment shows that QST works in principle.

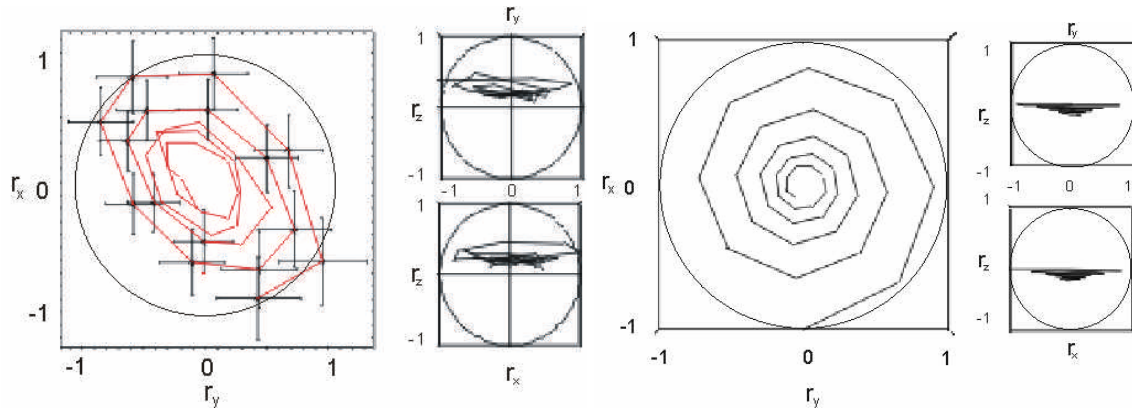


Fig. 4.19 Shows the movement of the Bloch vector. Left is the measurement and right is a simulation ($\gamma_1 = 1/5000ns$, $\gamma_\phi = 1/500ns$ and $\Delta = 0.005GHz$). The error bars are shown for the first twenty measurement.

From theory one would expect a helix.

In the measurement the Bloch vector turns around the z -axis in one direction, caused by the detuning and decreases, due to dephasing processes.

The measured helix is strongly squeezed. This can come from a bad calibration in the measurement pulses, which is not surprising because the analysis had to be done with low statistics. The signal follows a Poisson distribution in sample size therefore the lower sample size enlarged the error bar by a factor of ~ 1.5 . The instability of the Qubit might also enlarge the error bars additionally.

These facts are indicated by the size of the error bars. Here the relative error is approx. 50%, where it has been before at approx. 10%.

Anyway one can see that a helix predicted by theory could be fitted into the error bars as show in Fig. 4.20 (not a big surprise with this error bars).

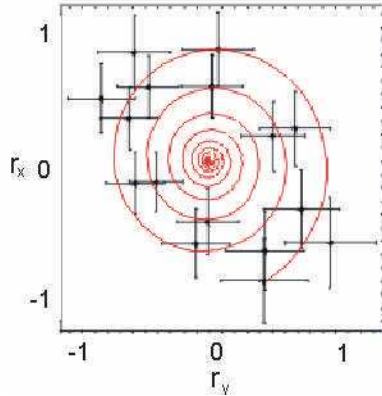


Fig. 4.20 The simulated trajectory can be placed into the error bars as shown for the first twenty measurement.

It is likely that the results look much nicer, if the experiment is redone when the Qubit is calmer.

The setups for the measurements were:

For this measurement the operations pulses were applied in parallel. The pulses were set to $\pi/2$ pulses by adjusting the amplitudes as usual were not exact $\pi/2$. The pulse length was 10 ns for each pulse. The spec. power was 13 dBm at 450 mV. The spectroscopy frequency was adjusted at 3.704 GHz.

The RF power was -26 dBm (30 photons in the cavity).

The time between the preparation pulse and the tomography pulse was increased in 25 ns steps [4].

A schematically plot of the pulse sequence is given in Fig. 4.21.

The underground was determined by projecting $|0\rangle$ on the state $|1\rangle\langle 1|$ and then averaging the response.

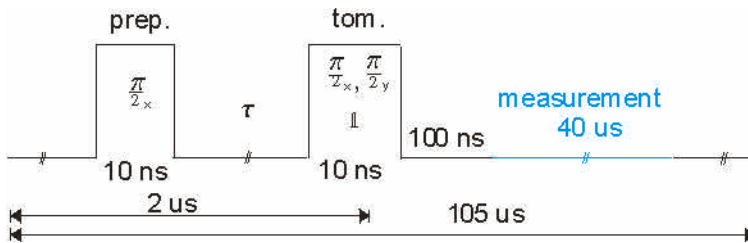


Fig. 4.21 Shows the parallel pulse sequence. The pulses have fix length but vary in their amplitude. The first pulse prepare the state and the second is for tomography. The time length between the pulses vary in 25 ns steps.

4.5.2 Pattern files

A sequence file contributes again of three different parts first the four calibrations pulses, second 40 times three tomography pulses with different times between the pulses and thirdly thirty pulses for Rabi oscillation.

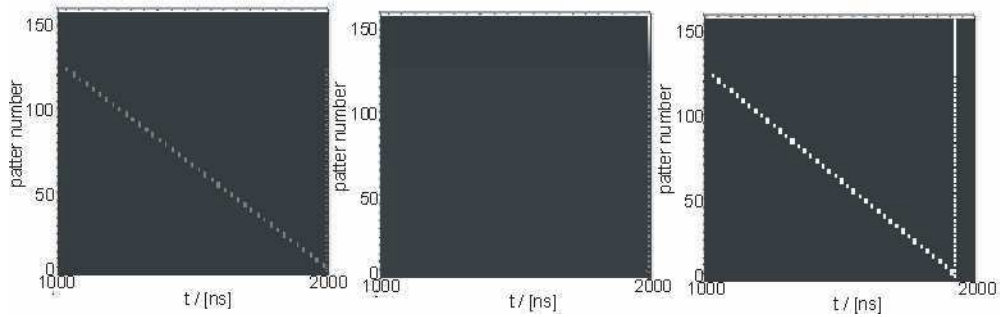


Fig. 4.22 Shows the used pattern files. The first two determine the operation pulses' amplitude. The pattern file has forty times four pulse for calibration, three for tomography and thirty for Rabi. The pulse length is constant 10 ns. The third turns the microwave generator one/off.

This pattern files are in one sequence file.

The three times forty pulses are used for the Ramsey experiment. The time between the preparation pulse and the tomography pulse increases in 25 ns time steps.

The sequence file should have been measured ten times and then averaged. However the Qubit jumped a lot and it was only possible to record a measurement where we could average five thousand times.

References

- [1] D. Schuster; PhD Dissertation Yale, 2006
- [2] J. Blatter; Lecture on Quantum Mechanic I and II, 2006
- [3] M. Steffen, M. Ansmann, R. McDermott, N. Katz, R. Bialczak, E. Lucero, M. Neeley, E. Weig, A. Cleland, J. Martinis; PRL 97, 050502, 2006
- [4] L. Steffen; Semesterarbeit ETH, 2007
- [5] Y. Liu, L. Wei, F. Nori; PRB 72, 014547, 2005
- [6] A. Houck, D. Schuster, J. Gambetta, J. Schreier, B. Johnson, J. Chow, J. Majer, L. Frunzio, M. Devoret, S. Girvin, R. Schoelkopf; Nature 445, 7127, 2007
- [7] C. Kittel; Einführung in die Festkörperphysik; Oldenbourg, 14 Edition, 2005
- [8] A. Blais, RS. Huang, A. Wallraff; PRA 69 (6), 062320, 2004
- [9] L. Frunzio, A. Wallraff, D. Schuster; IEEE Appl. Sup. 15 (2), 860-863, 2005